On the orbits that generate the X-shape in the Milky Way bulge

Caleb G. Abbott,[1,2]★ Monica Valluri,[1]★ Juntai Shen[3,4] and Victor P. Debattista[5]

[1]*Department of Astronomy, University of Michigan, Ann Arbor, MI 48109, USA*
[2]*Department of Physics and Astronomy, Georgia State University, Atlanta, GA 30303, USA*
[3]*Key Laboratory for Research in Galaxies and Cosmology, Shanghai Astronomical Observatory, Chinese Academy of Sciences, Shanghai 200030, China*
[4]*College of Astronomy and Space Sciences, University of Chinese Academy of Sciences, 19A Yuquan Road, Beijing 100049, China*
[5]*Jeremiah Horrocks Institute, University of Central Lancashire, Preston PR1 2HE, UK*

ABSTRACT

The Milky Way (MW) bulge shows a boxy/peanut or X-shaped bulge (hereafter BP/X) when viewed in infrared or microwave bands. We examine orbits in an *N*-body model of a barred disc galaxy that is scaled to match the kinematics of the MW bulge. We generate maps of projected stellar surface density, unsharp masked images, 3D excess-mass distributions (showing mass outside ellipsoids), line-of-sight number count distributions, and 2D line-of-sight kinematics for the simulation as well as co-added orbit families, in order to identify the orbits primarily responsible for the BP/X shape. We estimate that between 19 and 23 per cent of the mass of the bar in this model is associated with the BP/X shape and that the majority of bar orbits contribute to this shape that is clearly seen in projected surface density maps and 3D excess mass for non-resonant box orbits, 'banana' orbits, 'fish/pretzel' orbits and 'brezel' orbits. Although only the latter two families (comprising 7.5 per cent of the total mass) show a distinct X-shape in unsharp masked images, we find that nearly all bar orbit families contribute some mass to the 3D BP/X-shape. All co-added orbit families show a bifurcation in stellar number count distribution with distance that resembles the bifurcation observed in red clump stars in the MW. However, only the box orbit family shows an increasing separation of peaks with increasing galactic latitude |*b*|, similar to that observed. Our analysis suggests that no single orbit family fully explains all the observed features associated with the MW's BP/X-shaped bulge, but collectively the non-resonant boxes and various resonant boxlet orbits contribute at different distances from the centre to produce this feature. We propose that since box orbits (which are the dominant population in bars) have three incommensurable orbital fundamental frequencies, their 3D shapes are highly flexible and, like Lissajous figures, this family of orbits is most easily able to adapt to evolution in the shape of the underlying potential.

Key words: Galaxy: bulge – Galaxy: kinematics and dynamics – Galaxy: structure.

1 INTRODUCTION

Observations of bars in edge-on extragalactic disc galaxies often show a distinct boxy-peanut (BP) shaped bulge, which reveals a clear X-shaped structure when the images are subjected to unsharp masking. These structures are now observed in about 45 per cent of edge-on disc galaxies (Burbidge & Burbidge 1959; Shaw 1987; Combes et al. 1990; Lütticke, Dettmar & Pohlen 2000; Laurikainen et al. 2011), which if one accounts for the range of possible viewing angles, suggests that these structures are very common.

In the Milky Way (MW), Blitz & Spergel (1991) inferred the existence of a bar from 2.4 μm observations of the Galactic Center

(GC) region. A peanut-shaped bulge was first clearly seen in the multiparameter model of the *COBE*/DIRBE images of the Galactic bulge (Freudenreich 1998). Further evidence for an X-shaped bulge was inferred from the bifurcation in red clump (RC) star counts in the 2MASS and OGLE-III surveys (Skrutskie et al. 2006; McWilliam & Zoccali 2010; Nataf et al. 2010) and confirmed by Ness et al. (2012). These observations showed that at the Galactic coordinates *l* = 0° and |*b*| > 5°, the distribution of the RC stars splits into two distinct peaks, a bright peak on the near-side of the GC, referred to as the 'bright red clump' (BRC) and fainter peak on the far side of the GC, the 'faint red clump' (FRC). McWilliam & Zoccali (2010) interpreted these two clumps as evidence for an X-shape within the MW bar. This was confirmed shortly thereafter by Saito et al. (2011). An excellent demonstration of the existence of a X-shaped bulge is seen in the 3D distribution of

RC stars from the VVV survey (Wegg & Gerhard 2013). Recently, Ness & Lang (2016) have shown, by constructing an image of the MW bulge from an independent co-adding of publicly available *WISE* data, that MW bulge shows a distinct X-shaped structure in the projected stellar distribution even without unsharp masking.

Using Fourier harmonic fitting to the isophotal distributions of the sample of BP/X galaxies, Ciambur & Graham (2016) recently showed that the peanut/X-shapes embedded in near edge-on discs are best described not by the fourth Fourier harmonic (B_4), which is usually used to distinguish between boxy and discy bulges, but by the sixth Fourier harmonic (B_6). Furthermore, they use five quantitative metrics to describe the strength of the BP/X shape and show that the length and strength of the peanut increase with the rotation velocity of the disc.

BP bulges with vertical X-shaped structures are found to arise naturally in simulations of bars as a result of the asymmetric buckling instability (Raha et al. 1991; O'Neill & Dubinski 2003; Martinez-Valpuesta & Shlosman 2004; Bureau & Athanassoula 2005; Debattista et al. 2005, 2006). This instability typically occurs as the bar strengthens and when the velocity dispersion along the length of the bar (σ_x) significantly exceeds the vertical velocity dispersion (σ_z), (e.g. when $\sigma_z/\sigma_x \lesssim 0.4$; Araki 1985; Martinez-Valpuesta, Shlosman & Heller 2006). The instability causes a redistribution of kinetic energy from the plane of the disc resulting in a significant increase of the thickness of the bar, giving it the familiar BP shape (Pfenniger & Friedli 1991). The X-shaped structure seen in projection and in unsharp masked images is probably more peanut-like in 3D, and the visual perception of an X-shape in projection is enhanced by the pinched, concave inner isodensity contours (Li & Shen 2015). This BP/X-shape can qualitatively reproduce the observed bimodal distributions in the number counts of RC stars along the line of sight that were used as evidence for the discovery of the X-shape. Indeed, several studies comparing *N*-body simulations of bars with the observed spatial distributions and line-of-sight velocity distributions of RC stars in the MW (Shen et al. 2010; Li & Shen 2012; Vásquez et al. 2013; Gardner et al. 2014; Nataf et al. 2015; Qin et al. 2015) argue that the buckling of bars that gives rise to the BP shape seen in external galaxies is also responsible for the observed X-shaped structure in the MW bulge. Alternative mechanisms such as resonant trapping of stars on vertical inner Lindblad resonances (Combes & Sanders 1981; Combes et al. 1990; Quillen 2002; Quillen et al. 2014) and resonant trapping of disc material around the stable 3D periodic orbits associated with vertical 2:1 and 4:1 resonances (Patsis & Xilouris 2006) may also contribute. While most boxy bulges are generally associated with bars, axisymmetric boxy bulges can also exist (Rowley 1988; Patsis et al. 2002a).

An obvious question that arises is whether one or more specific orbit families in self-consistent bars are responsible for the BP bulge and/or the X-shape. The standard view of orbital structure of bars has held that the dominant families of bar orbits are quasi-periodic or regular orbits that arise from stable periodic prograde x1 and x2 orbits (e.g. Contopoulos & Papayannopoulos 1980; Athanassoula et al. 1983). For example, the vertical bifurcation of the x1 family, e.g. the 2:−2:1[1] resonant orbit family (referred to hereafter as the 'banana' orbit family, often referred to in the literature as

'x1v1' orbits) is widely considered to be the backbone of BP/X bulges seen in edge-on buckled bars (Pfenniger & Friedli 1991; Patsis, Skokos & Athanassoula 2002b; Skokos, Patsis & Athanassoula 2002a; Athanassoula 2005). Skokos, Patsis & Athanassoula (2002b) also found that in a model without 2:−2:1 orbits, the bar was supported by orbit families connected with *z*-axis orbits. Patsis & Katsanikas (2014a,b) also present a dynamical mechanism for building X-shaped peanuts with families of periodic orbits that are not bifurcations of x1 orbits.

Recently (e.g. Qin et al. 2015), it has been argued that it is difficult to clearly identify a single orbit family that reproduces both the spatial and kinematical distributions associated with the X-shape in the MW bulge. Portail et al. (2015a) constructed models of the Galactic bulge that fit the spatial distribution of bulge stars from the VVV survey (Wegg & Gerhard 2013) and kinematical data from the Bulge RAdial Velocity Assay (BRAVA; Rich et al. 2007; Kunder et al. 2012). By analysing the orbital structure of their self-consistent made-to-measure models and *N*-body models, Portail, Wegg & Gerhard (2015b) argued that since the 2:−2:1 vertical resonance of the x1 orbit family appears primarily in the outer parts of bars, they cannot explain the X-shape in the MW bar that is observed over a range of distances from the centre of the bar. Instead, they proposed that resonant boxlet orbits associated with the 3:0:−5 resonance (which they term 'brezel' orbits) are primarily responsible for the X-shape. They further conclude that ∼40–45 per cent of the stellar orbits in the bulge/bar contribute to the X-shape.

The fraction of stellar mass associated with the X-shape has been estimated from unsharp masking by Li & Shen (2012) to about 7 per cent of the bulge mass. In contrast, Portail et al. (2015a) estimate the 'excess mass' lying outside ellipsoids and infer that 20–25 per cent of the mass of the bulge is associated with the X-shape. These differences are most probably due to the differences in the methods used to compute the mass associated with the X-shape.

We recently carried out a comprehensive analysis of a representative sample of orbits drawn from the self-consistent particle distribution of two *N*-body bars (Valluri et al. 2016, hereafter V16). We showed that the dominant bar orbit family (comprising ∼60 per cent of bar orbits) is the box orbit family (otherwise referred to as the 'non-resonant x1 orbit family' in 3D potentials) that originates from perturbations of the linear long-axis orbit. This box orbit family is well known from studies of stationary triaxial ellipsoids where it is the dominant family (de Zeeuw 1985; Binney & Tremaine 2008). In the frame co-rotating with an *N*-body bar, these box orbits are modified only slightly by the pseudo-forces arising from the rotating potential. Furthermore, V16 showed that the vertical bifurcation of the x1 orbit, the 2:−2:1 'banana' orbits comprises only about 3 per cent of all bar orbits and is found primarily in the outer half of the bar. This latter result is consistent with the findings of Portail et al. (2015b). V16 found that the most important resonant boxlet family (comprising about ∼6 per cent of orbits) in *N*-body bars[2] is associated with the 3:−2:0 resonance that we refer to as 'fish/pretzel' orbits. *N*-body bars were also found to contain long-axis tube orbits (4–8.5 per cent), a small fraction of short-axis tube orbits (i.e. orbits originating from retrograde x4 orbits and prograde x2 orbits) and a significant fraction (18–22 per cent) of chaotic

---

[1] We use orbital fundamental frequencies in Cartesian coordinates to define resonant orbits: i.e. orbits that are resonant satisfy the resonant condition $\Omega_x : \Omega_y : \Omega_z = l : m : n$, where *l*, *m*, *n* are small integers. The sign associated with an integer depends on the signs of the slope and intercept of a resonance line when plotted on a frequency map.

[2] V16 showed that this is also the most important resonant boxlet family in rapidly rotating prolate triaxial potentials described by the Dehnen profile (Dehnen 1993).

orbits. The precise fractions of orbits associated with different families are expected to be somewhat dependent on the details of the bar potential, with the range of orbital fractions listed above arising in the two models discussed in V16.

In this paper, we re-examine regular orbits in one of the *N*-body simulations previously classified and analysed in V16. Although we found a significant fraction of chaotic orbits in our *N*-body bars, we do not examine them here because their spatial distributions evolve with time implying that the inferred spatial distribution is sensitive to the choice of orbital integration time. However, we note in passing that on short orbit integration times, the majority of chaotic orbits in our models behave like non-resonant box orbits.

We use four different diagnostics to compare the full simulation with co-added orbits from different orbit families: (1) projected surface density distribution and unsharp masked images of these density distributions; (2) the 3D 'excess mass' that lies outside concentric ellipsoids; (3) bifurcation in the stellar number count distributions along several lines of sight and variation of the separation between the peaks of these distributions as a function of galactic latitude *b* and (4) 2D maps of the separation in the mean line-of-sight velocity (ΔV_{los}) for RC stars on the near and far sides of the GC. The goal of this analysis is to determine the types of orbits that give rise to the BP and/or the X-shapes observed in both *N*-body bars and real galactic bars. Although our models have not been specifically tailored to fit the MW, they describe several of the observed features extremely well and therefore yield useful insights into observations of structural and kinematical features in the MW bulge.

This paper is organized as follows. In Section 2, we describe the bar simulations from which the line-of-sight kinematics were derived and in which orbits were computed. We also briefly recap the main results of V16 describing the orbit families in *N*-body bars. In Section 3, we present comparisons between the full simulation and co-added orbits in different families and qualitatively compare these with MW data where available. We summarize our results and conclude in Section 4.

2 SIMULATIONS AND ANALYSIS METHODS

2.1 *N*-body bar models

We examine two *N*-body bar models both arising from the same set of initial conditions. The models are almost identical to those used by one or more authors of this paper in the past (Shen & Sellwood 2004; Brown et al. 2013; V16). What follows is a brief description of the simulations and the orbit analysis methods employed. For a more detailed description of the simulation methods and the initial conditions, the reader is referred to the above papers. The initial disc galaxy contains ~2.8 million particles described by a Kuzmin density profile with disc mass M_{d} and radial length-scale R_{d}. Particles were given initial velocities such that the Toomre parameter is $Q \sim 1.5$, making the disc unstable to bar formation. The disc is embedded in a static, spherical dark matter halo described by a logarithmic potential. While it is well known that there are differences in the growth rate and strength of bars that form in live dark matter haloes and static dark matter haloes (Athanassoula 2002), Shen & Sellwood (2004) found little difference in the evolution of bar orbits in live and static dark matter haloes with the same density profile. Furthermore, a recent study of a bar in a live halo with a cusp finds substantially similar orbital structure (Gajda, Łokas & Athanassoula 2016) to that found by V16, hence our results are expected to be fairly typical for bars of similar strength to those studied here.

The initial conditions were evolved using a 3D, cylindrical, polar grid-based *N*-body code (Sellwood & Valluri 1997; Sellwood 2014). The bar forms, grows in strength and then buckles. After the buckling phase, the bar strength saturates at $t \sim 700$ time units and thereafter the bar maintains a nearly steady rotation speed and bar strength. A frozen snapshot of the bar at $t = 700$ units is therefore used to represent a pure bar and is referred to as 'Model A'. This simulation is evolved further as a central point mass (representing a supermassive black hole – SMBH – with an $M_{\text{BH}} = 0.0002\, M_{\text{d}}$) is grown adiabatically at the centre. Transients associated with the growth of the central point mass dissipate by $t = 1200$. The snapshot of the simulation at this time is referred to as 'Model C'.

Following standard practice, the coordinate system for the model is defined with the *x*-axis along the length of the bar, the *y*-axis is in the plane of the disc perpendicular to the *x*-axis and the *z*-axis is perpendicular to the disc.

The simulations and co-added orbits were analysed for two different orientations of the bar: (a) an edge-on disc very far away from the observer with the bar oriented perpendicular to the line of sight to the galaxy (i.e. bar seen side-on) and (b) a configuration designed to mimic the orientation of the MW bar as seen from Sun [referred to hereafter as 'the heliocentric rotated' (HCR) frame].

In the HCR frame, the simulated bar was rotated such that the long-axis of the bar lies at 27° to our line of sight to the GC to match the orientation of the MW bar of 27° ± 2° (Wegg & Gerhard 2013). The distance of Sun from the GC is assumed to be 8 kpc (e.g. Eisenhauer et al. 2003). In this frame, the bar is not perpendicular to our line of sight to the GC, hence we defined a new coordinate system: (β, α, z) with the origin at the GC and with the positive α-axis oriented along the line connecting the GC to Sun and the β-axis perpendicular to our line of sight to the GC with positive β values associated with positive longitudes. The definition of the *z*-axis is the same in both coordinate systems.

The simulations were run in units with $G = M_{\text{d}} = R_{\text{d}} = 1$, where *G* is Newton's gravitational constant. Using standard dimensional analysis, the unit of time is $t_{\text{dyn}} = (R_{\text{d}}^3/GM_{\text{d}})^{1/2}$. In order to compare the simulations with observations of the MW bar/bulge, it was necessary to convert the simulation units to physical units. The bar length was estimated using two different methods. The first method measures the $m = 2$ Fourier moment amplitude and the second method measures the phase in annuli. A lower limit on the length of the bar is obtained by determining the length at which the strength of the $m = 2$ mode drops to 20 per cent of the peak amplitude. While this is a reasonable estimate, it is generally considered to be a lower limit to the bar length. The measurement based on the phase determines the bar length to be the radius at which the phase deviates by more than 10° from a constant. This tends to overestimate the bar length. We use a simple average of both estimates to set the length of the bar to 3.9 units in Model A and 4.5 units in Model C. We compare these values to recent estimates of the length of the MW bar (5 ± 0.2 kpc for the full bar; Wegg, Gerhard & Portail 2015) and thereby choose R_{d} to be 1.28 kpc for Model A and 1.1 kpc for Model C.

The parameter representing the disc mass, M_{d} was determined by fitting the simulations to the MW bulge line-of-sight kinematical data (V_{los} and velocity dispersion σ_{los}) obtained by the BRAVA survey at 77 different pointings (Rich et al. 2007; Kunder et al. 2012). We determine the best-fitting value of M_{d} by varying this quantity (with R_{d} fixed as described above) and computing the resulting χ^2 of the fit to all the kinematical data (in a manner similar to that used by Gardner et al. 2014, hereafter G14). This was done separately for Model A and Model C since the growth of
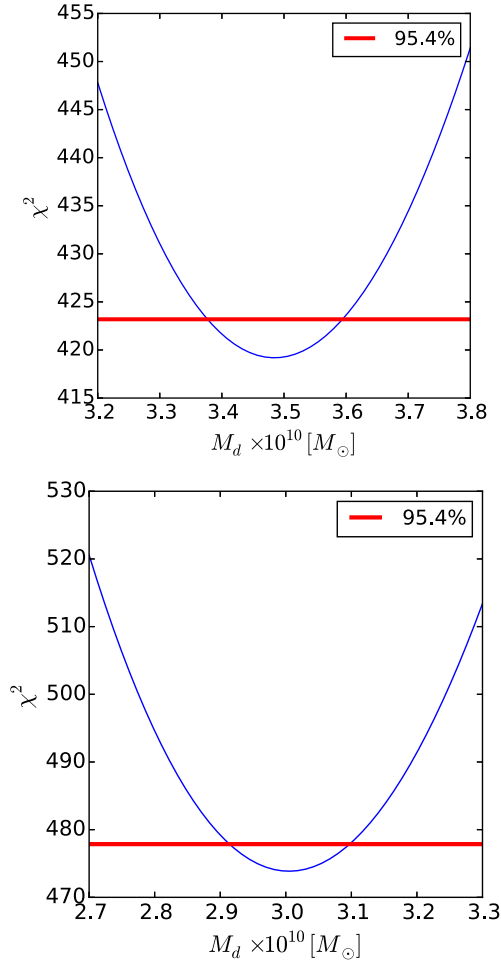
Figure 1. χ^2 of the fit to the BRAVA kinematical data (Rich et al. 2007; Kunder et al. 2012) shown in Fig. 2 as a function of M_d for Model A (top) and Model C (bottom). Horizontal red lines show the 3σ confidence intervals in $\Delta\chi^2$ (relative to the minimum) for one degree of freedom. The minimum χ^2 was obtained for $M_d = 3.48 \times 10^{10}$ M$_\odot$ (for Model A) and for $M_d = 3.01 \times 10^{10}$ M$_\odot$ (for Model C).

the black hole and the angular-momentum transfer induced by the bar increases the density of stars (therefore the velocity dispersion) in the nuclear region. Fig. 1 shows χ^2 of the fit to all the kinematical data as a function of M_d for Model A (top) and Model C (bottom). The horizontal red lines mark the 3σ $\Delta\chi^2$ error region. The best-fitting values of M_d were 3.48×10^{10} ($\pm 5 \times 10^8$) M$_\odot$ (Model A), and 3.01×10^{10} ($\pm 5 \times 10^8$) M$_\odot$ (Model C). In Model C, this value of M_d gives an $M_{BH} = 6.02 \times 10^6$ M$_\odot$, making it roughly 1.6 times the mass of the MW black hole. With these values for R_d and M_d, $t_{dyn} = 3.69$ and 3.17 Myr for Model A and C, respectively. The χ^2 of the fit to kinematics for the two models are $\chi^2 = 419$ (Model A) and $\chi^2 = 473$ (Model C) giving reduced χ^2 of 2.7 and 3.1, respectively, signifying only moderately good fits to the data. We note that since the bar simulations analysed in this paper were not explicitly designed to fit the MW bar, the orbit distributions in our simulations may not exactly represent those in the MW.

Fig. 2 shows the BRAVA data (V_{los} and σ_{los}, green points) at $l = 0°$ and $b = -4°, -6°, -8°$, with the best-fitting models shown as solid curves with 3σ bootstrap error bands (Model A blue/light blue, Model C red/pink). Bootstrap errors on the fits were obtained

by taking 100 random re-samplings of simulation particles in each bin (allowing for repetition) that contained at least 100 simulation particles. Bins with fewer than 100 particles were not fitted.

Fig. 3 shows the projected surface density distributions and unsharp masked images (which highlight the X-shape). Unsharp masked images were obtained by taking the full projected particle distribution, binning the particles on a 70×70 pixel grid and then smoothing the binned density distribution with a square kernel (4 pixels wide) that is moved over the entire grid. The smoothed image is then subtracted from the original image to obtain the unsharp masked image. The unsharp masked images are re-scaled to provide the best image contrast.

Both models show a clear BP/X-shaped bulge in projected surface density (left-hand column) and the unsharp masked images (right-hand column) clearly reveal an off-centre X-shape (according to the classification of Bureau et al. 2006). We note that although the off-centre X-shape is also observed in the MW, the strength of the X-shape in our bars maybe somewhat weaker than that observed in the MW (Wegg & Gerhard 2013; Portail et al. 2015a), hence the detailed orbital structure of the MW bar may differ somewhat from the one presented here.

Following a method similar to that discussed in Portail et al. (2015a), we construct 3D isodensity surfaces for both of our *N*-body models. This is done by binning all the particles in the bar on a 3D Cartesian grid comprising $40 \times 40 \times 40$ bins. We then identify 10 equally spaced isodensity levels. Starting from the highest isodensity surface and working outwards for each surface, we define the largest ellipsoid that can be enclosed entirely within a given isodensity surface. The mass enclosed within this ellipsoid is subtracted from the mass enclosed within the isodensity surface to obtain the residual 'excess mass' associated with the BP/X shape. This mass was found to be 23 per cent of the total mass of the bar for Model A and 19 per cent for Model C, consistent with values found by Portail et al. (2015a, 24^{+5}_{-4} per cent). This excess-mass distribution projected on to the x–z plane is shown in Fig. 4. We find that the residual mass distribution in both Models A and C is peanut-shaped unlike the residual mass distribution shown in Portail et al. (2015a, see fig. 18) that shows a distinct X-shape in the x–z projection. However, our results are completely consistent with the results obtained by Li & Shen (2015).

The terms 'BP' and 'X-shaped bulge' are generally used interchangeably in the literature. Our analysis above shows that while this is probably justified, the process by which this structure is identified, e.g. direct examination of projected density, unsharp masking or analysis of 3D spatial distribution, appears to affect conclusions about how much mass is associated with it.

Vásquez et al. (2013) obtained line-of-sight velocities and proper motions for stars belonging to the BRC and the FRC. These authors found that the two arms of the X-shape intersect the line of sight from the Sun to the GC at $l = 0°$ and $|b| > 4°$. Vásquez et al. (2013) found that the velocity distribution of stars in the BRC is skewed towards negative V_{los} while the velocity distribution of stars in the FRC is skewed towards positive V_{los}. Cumulative distribution functions (CDF) of the heliocentric radial velocities of the BRC and FRC stars show that the median velocities of these two distributions differ by ~ 50 km s^{-1}. Their comparison with a simulated bar (from Debattista et al. 2005, see also G14) shows that this difference in the CDFs of 'Near' and 'Far' side stars is a characteristic of the X-shape.

We searched for a similar feature in V_{los} in our simulation by splitting stars in our simulations into a near group and a far group by defining star particles as 'Near' if $\alpha < 8$ kpc and defined star
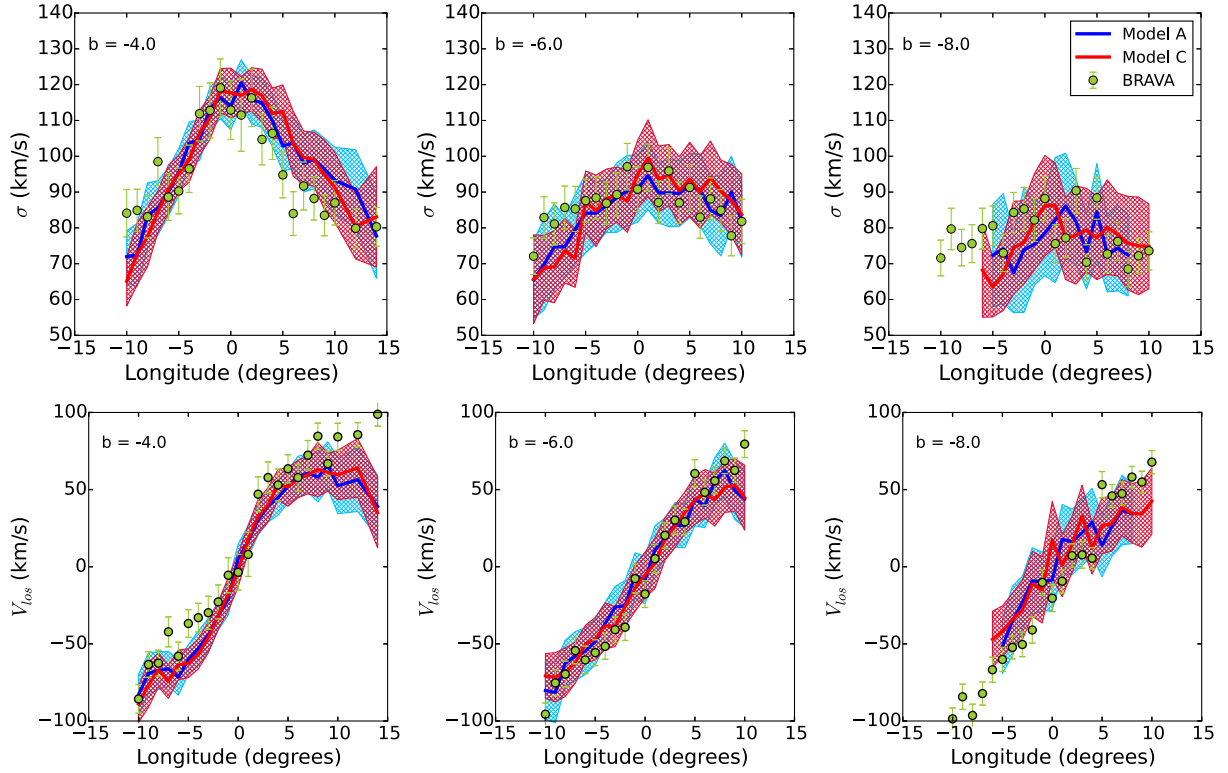
Figure 2. The fit to BRAVA data (green points) for the best-fitting M_d values are shown for $b = -4°, -6°, -8°$ for Model A (blue solid curves with light blue 3σ bootstrap error bands) and Model C (red solid curves with pink 3σ bootstrap error bands). Bins with fewer than 100 particles (e.g. for $b = -8°$, $-12° < l < -6°$) were not included in the fit.

particles as belonging to the 'Far' group if $\alpha > 8$ kpc. A similar process of splitting the data into a 'Near' group and a 'Far' group was also carried out for orbits in Model A. We note that this is a very simplistic way to attempt to reproduce the BRC and the FRC that does not account for magnitude limits of the observations or extinction effects, nor does it realistically account for a possible dependence on stellar populations and is therefore meant only to be a crude proxy for the observed velocity distributions. Note that similar cuts have been used by others in the comparison of simulations to data (Li & Shen 2012; Vásquez et al. 2013; Debattista et al. 2017).

Fig. 5 shows Model A (top row) and Model C (bottom row) in the HCR frame. The leftmost column shows a surface density map of all stars in the two bars from our heliocentric point of view. The asymmetry in the shape of the bulge due to the near-side of the bar being much closer to us is clearly seen and is similar to that observed in the MW (Wegg & Gerhard 2013). The second column shows histograms of V_{los} for 'Near' stars (red) and 'Far' stars (blue) at $l = 0°$, $b = -6°$ with solid red and blue lines showing the mean velocities of the two distributions obtained by Gaussian fitting. It is clear that the 'Near' (red) histogram peaks at negative V_{los} values as in the case of the BRC while the peak of the 'Far' (blue) histogram is at slightly more positive V_{los}. The difference in the mean velocities of 'Near' and 'Far' side stars is defined as $\Delta V_{los} = \langle V_{los} \rangle_{Near} - \langle V_{los} \rangle_{Far}$. At $l = 0°, b = -6°$, $\Delta V_{los} = 24.3$ km s^{-1}(Model A) and $\Delta V_{los} = 28.4$ km s^{-1}(Model C). The third column in this figure shows the CDFs of these two V_{los} histograms. The overall behaviour of the CDF of the 'Near' and 'Far' side stars in the third column is qualitatively similar to the BRC and FRC stars observed by Vásquez et al. (2013)

(although the separations in our simulations of 24–28 km s^{-1} are significantly smaller than the observed separation of ~50 km s^{-1}), perhaps because the strength of the X-shape in our bar is weaker than in the MW.

G14 showed that 2D maps of ΔV_{los} reveal kinematic differences between simulations with and without X-shapes. In particular, they found that a model with a strong X-shape (e.g. their model B3) showed an asymmetric ring-like structure populated with negative ΔV_{los} similar to that seen in the fourth column of Fig. 5 surrounding an inner circular region centred on $l = 0°, b = 0°$ where $\Delta V_{los} \sim 0$ or slightly positive (note that G14 used a colour scheme that is the opposite of that used in this figure). G14 also found that other types of kinematic maps (e.g. showing σ_{los}, or galactocentric azimuthal velocities and velocity dispersions) were not able to distinguish between models with and without X-shapes. We also made maps of σ_{los} and azimuthal velocities for both the full simulations and individual orbits and found them to be uninformative hence do not include them here.

Fig. 5 also shows that there is very little difference between Model A and Model C in either spatial or kinematic distributions. Since the SMBH in Model C (which is about 1.6 times more massive than the SMBH located at the GC) produces no perceptible difference from Model A (without an SMBH), we conclude that a BH of this low mass does not significantly alter the dynamical structure of the bulge and hence in the sections that follow, we confine the discussion to orbits in Model A. We note that V16 and Brown et al. (2013) analysed a model with a 10 times more massive SMBH (referred to as Model B) and found that the more massive SMBH does in fact alter the orbital structure in the nuclear region and produces slightly
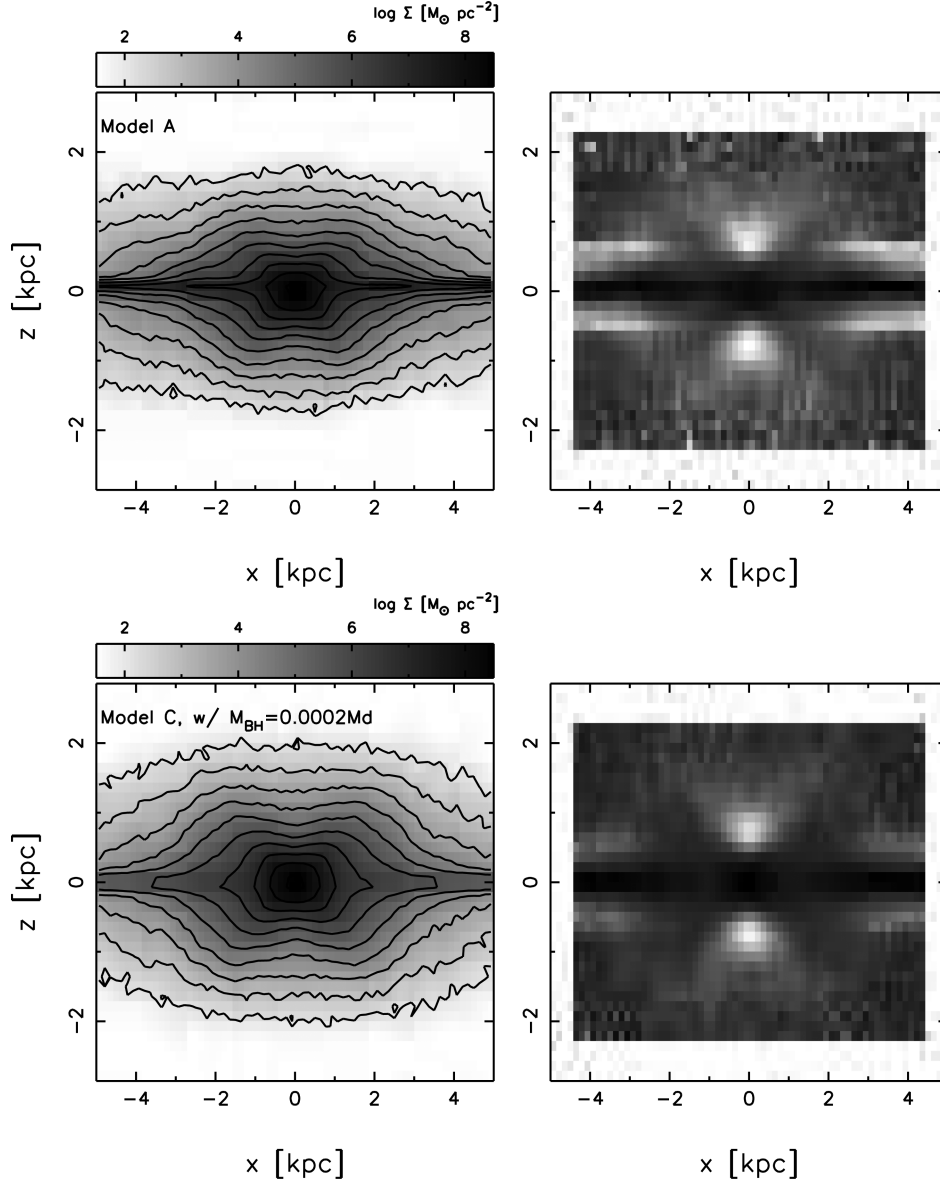
Figure 3. Projected surface mass density (left-hand column) and unsharp masked images (right-hand column) to highlight the X-shape in Model A (top row) and Model C (bottom row) when the bar is observed in an edge-on disc with bar perpendicular to our line of sight.

different kinematical signatures. Since this larger black hole mass is not relevant to the MW, we do not show results for Model B here.

2.2 Orbits

Orbits of 10 000 randomly selected particles from the self-consistent particle distribution for Model A were integrated starting from initial conditions corresponding to the positions and velocities of particles in the snapshot at $t = 700$ (after the bar growth largely saturates). The orbits were integrated in Cartesian coordinates in the frozen potential of the full simulation, after taking into consideration the appropriate Coriolis and centrifugal pseudo-forces determined by the pattern frequency Ω_p of the bar. The pattern frequency of the bar in Model A in program units is 0.117, which for our choice of physical units gives a pattern frequency $\Omega_p = 47.98$ km s^{-1} kpc^{-1}. The most recent estimate (Portail et al. 2017) of the pattern frequency of the MW bar is $\Omega_p = 39.0 \pm 3.5$ km s^{-1} kpc^{-1} (for a bar length

5.3 $\pm$ 0.36 kpc). These differences in pattern frequency (as well as differences in the strength of the bar) could account for some of the differences between the observations and the model seen in Fig. 2.

All orbits were integrated for 1000 time units (equal to 3.69 Gyr) in the rotating frame and saved at 20 000 equally spaced time intervals. Each orbit was then analysed using a spectral analysis code (Valluri & Merritt 1998; Valluri et al. 2010) and the fundamental orbital frequencies were used to classify orbits using the scheme described in V16.

As discussed by V16, orbits in *N*-body bars are essentially identical to orbits in triaxial ellipsoids, with the main difference being that they are modified by the pseudo-forces arising from figure rotation. Bar orbits belong to the same five main families found in triaxial ellipsoids: boxes, short-axis (*z*) tubes, inner and outer long-axis (*x*) tubes and chaotic orbits. V16 showed that ~60 per cent of bar orbits in two bar simulations were box orbits that are parented by
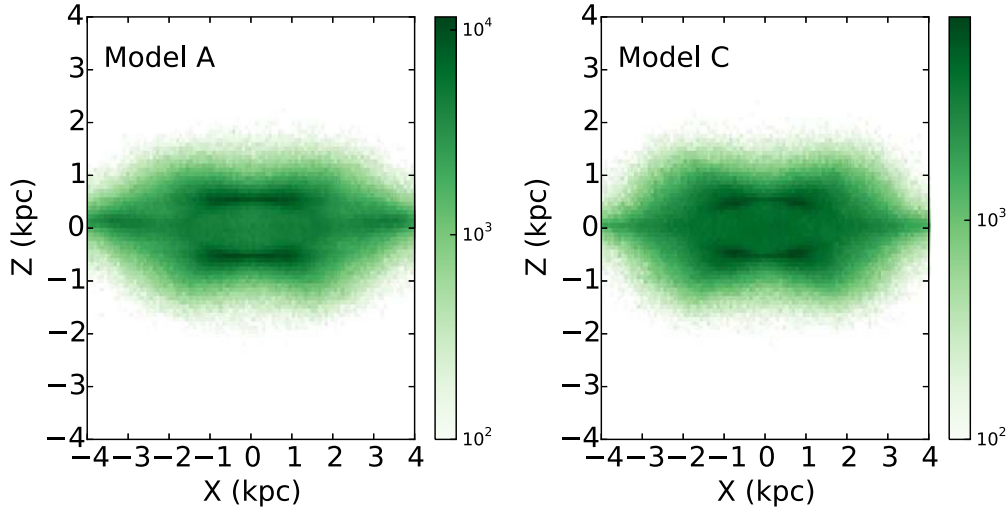
Figure 4. 2D projection of the 3D excess-mass density distributions for Model A (left) and Model C (right). The excess mass outside ellipsoids (see the text for details) shows a clear BP/X shape in both models. The colour gradient as shown in the bar on the right of each plot is in units of $M_\odot$ kpc^{-2}.
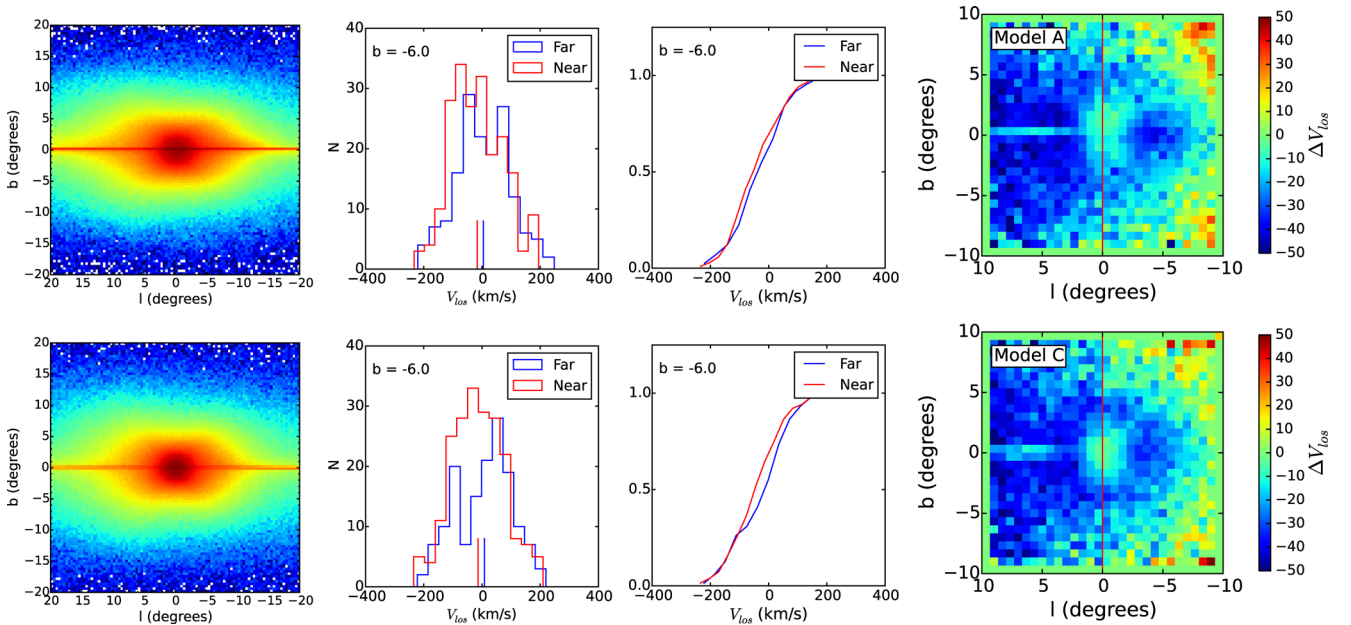

Figure 5. The first column shows projected stellar distribution of the two bars (Model A: top row, Model C: bottom row) oriented at 27° to our line of sight to the GC. An asymmetry similar to that observed for star counts in the MW bar (e.g. Wegg et al. 2015) is clearly seen. The second column shows histograms of V_{los} of stars at $(l, b) = (0°, -6°)$ for stars on the 'Near' and 'Far' sides of the GC shown in red and blue histograms, respectively. The mean velocities of these distributions (computed via Gaussian fitting) are marked by short red and blue vertical lines. The third column shows the CDF for these velocity histograms. The red CDFs rise slightly more rapidly than the blue CDFs showing that the distribution of stars on the near-side of the GC peaks at more negative V_{los} than stars on the far side. The final column shows 2D maps of ΔV_{los} (see the text for definition) that show the characteristic asymmetric ring-like structure with negative ΔV_{los} values surrounding a region with $\Delta V_{los} \sim 0$.

the linear orbit that oscillates along the x-axis (first row of Fig. 6). They also found a small fraction (8.5 per cent) of long-axis (x)-tube orbits (second row of Fig. 6). The orbit traditionally referred to as the 'prograde x1 orbit', and its vertical bifurcation the 2:−2:1 banana orbit is shown in third row of Fig. 6 (this family comprises 3 per cent of all bar orbits). V16 also identified higher order resonant 'boxlets', members of the box orbit family associated with the 3:−2:0 resonance and the 3:0:−5 resonance. The former, which we refer to as the 'fish/pretzel' resonance (although it is different

from the 3:0:−2 fish and 4:3:0 pretzel families found in stationary triaxial potentials) is shown in the fourth row of Fig. 6 and is the largest resonant family, comprising ∼6 per cent of bar orbits. Less than 2 per cent of orbits were associated with the 3:0:−5 'brezel' resonance (fifth row of Fig. 6) that was proposed by Portail et al. (2015b) as the backbone of the X-shape.

A small number of orbits in Model A are retrograde short-axis tube orbits (which are elongated along the y-axis of the model and resemble x4 orbits) and none of the orbits in this model were
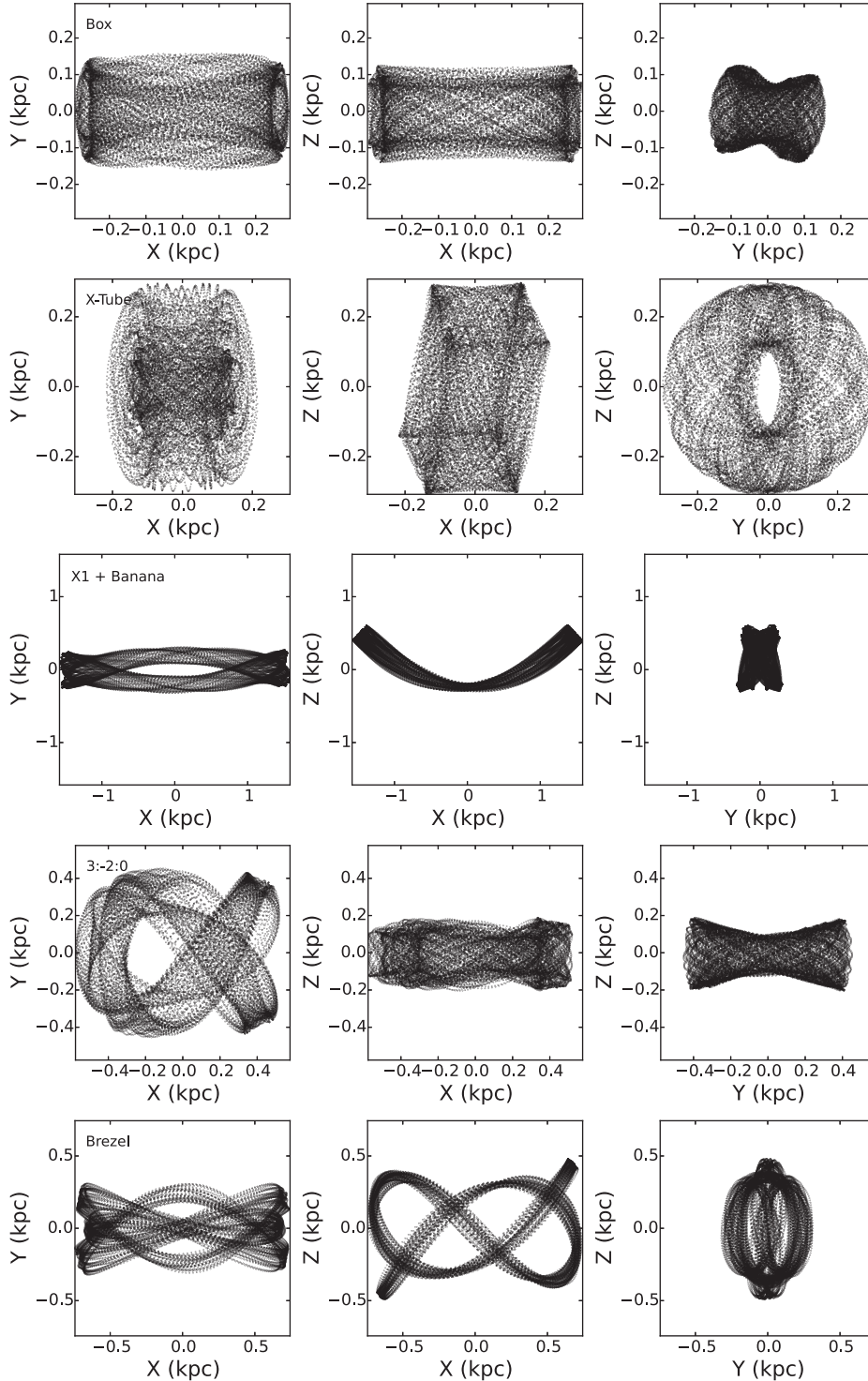
Figure 6. Three different projections of five different orbits in Model A. From the top to bottom: a box orbit, an *x*-tube orbit, a banana(x1v1) orbit (2:−2:1), a fish/pretzel orbit (3:−2:0) and a brezel orbit (3:0:−5).

associated with prograde x2 orbits. Our analysis of short-axis tubes reveals that they show neither a BP shape nor an X-shape in projection and do not have line-of-sight density or kinematical distribution consistent with MW observations and hence for the rest of this paper, this family is ignored. As mentioned previously, we also ignore chaotic orbits, since their shapes evolve with time, although at 18–20 per cent of bar orbits they are not an insignificant population.

3 RESULTS

3.1 Projected distributions and unsharp masking for orbits

With the orbit classifications from V16 in hand, we set about analysing each orbital family to determine which family (or families) is (are) primarily responsible for producing the BP/X-shape in this model. This was done by co-adding all orbits belonging to
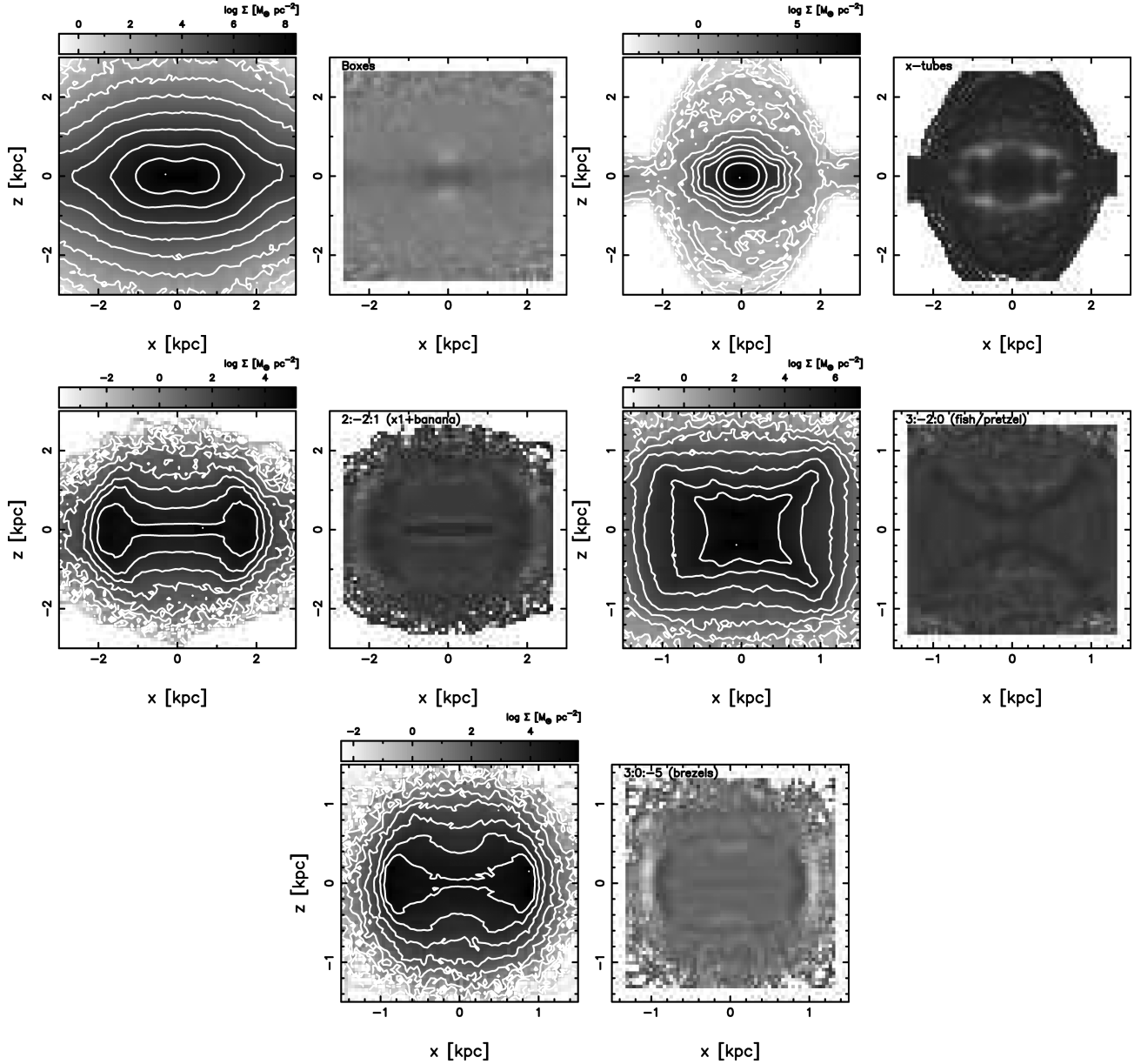
Figure 7. Each pair of panels shows projected surface mass density (left) and unsharp masked image (right) for five orbit families from Model A as labelled. The box orbits (top row left) and *x*-tube orbits (top row right) show a distinct peanut shape in projected surface density maps but no X-shape in unsharp masked images. Resonant 2:−2:1 x1+banana orbits (second row left) show a BP/X-shape in projected surface density map (left) but not in unsharp masked image (right) where it shows two shell-like structures at ±2 kpc. The resonant boxlet 3:−2:0 (fish/pretzel) orbits show a distinct X-shape both in projected surface density and unsharp masked images (second row right). The resonant 3:0:−5 (brezel) orbits show a peanut shape (left) and faint X-shape with two shell-like structures at ±1 kpc (right, third row).

a particular family and constructing the projected density distribution for that family. We are justified in superposing orbits in this manner because all orbits were integrated for the same amount of time and saved at the same time-steps and hence orbit superposition is akin to considering a large number of stars (on a given orbit) whose positions reflect the density distribution along the orbit. We present the projected X-shape only in the edge-on bar since it is most clearly observed in this orientation (but similar results were obtained in the HCR frame). The HCR projection is used for examining line-of-sight number counts and line-of-sight kinematics since we compare these metrics with observations for the MW.

As we saw in Fig. 3, the projected density distribution of the full simulation shows the BP shape while the process of unsharp masking best reveals the presence of the X-shape. We now make similar plots for each of the five different families by co-adding all members of a given family (Fig. 7). Each row shows co-added plots for two orbit families and for each family we show the projected surface density in the left-hand panel and the unsharp masked image on the right.

The box orbits (top row, two left-hand panels) show a distinct peanut shape and even a hint of an X-shape in the projected surface density plot but does not show an X-shape in the unsharp masked image.
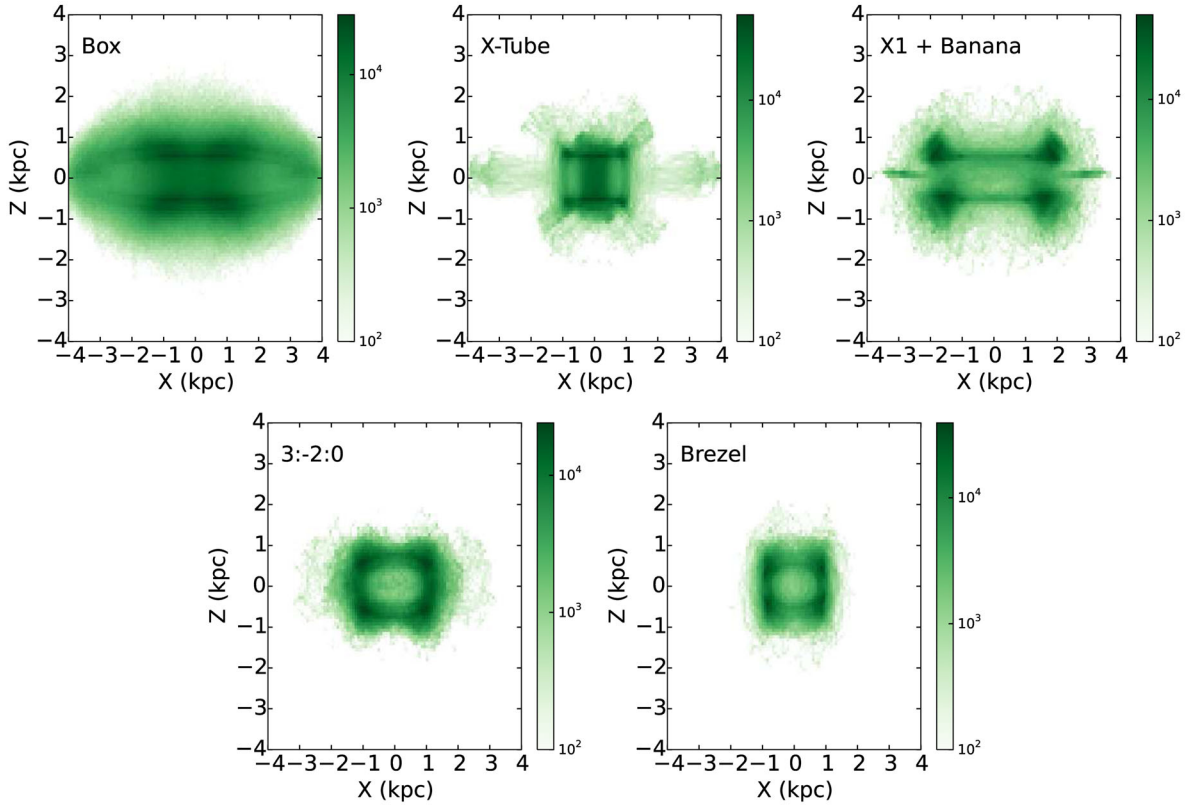
Figure 8. Projected excess-mass density on the *x*–*z* plane for each of the five orbit families from Model A as labelled. The colour gradient as shown in the bar on the right of each plot is in units of $M_\odot$ kpc^{-2}. The box orbits (top row left) and resonant 2:$-$2:1 x1+banana orbits (top row right) show a clear BP/X-shape at large radii. The *x*-tube orbits (top row middle) show a hint of an X-shape but at very low-density levels. Resonant boxlet 3:$-$2:0 fish/pretzel orbits (bottom row left) and resonant 3:0:$-$5 brezel orbits (bottom row right) show a BP/X-shape at small radii ($\leq$2 kpc).

The *x*-tubes (top row, two right-hand panels) show a small-scale peanut-shaped structure (within ±1 kpc) in both the full projection and in the unsharp masked image. This smaller scale peanut (along with the larger peanut produced by the boxes) might contribute to the nested peanuts recently observed by Ciambur & Graham (2016).

The x1+banana orbits (2:$-$2:1 resonance) clearly show a peanut shape, with a hint of a broad X-shape, in the projected surface density plot but the unsharp masked image shows no evidence of an X-shape. Rather, in the unsharp masked image, we see two shell-like structures perpendicular to the disc at ±2 kpc.

The two resonant boxlet families, the 3:$-$2:0 fish/pretzel (second row right) and the 3:0:$-$5 brezel (third row) show distinct X-shapes both in the projected surface density plots and in the unsharp masked images. In the case of the brezels, the X-shape is much broader and more diffuse and it also shows the double shell-like structure at ∼± 1 kpc similar to that seen for the x1+bananas.

It appears from the projected density plots that several families contribute to the BP shape (boxes, *x*-tubes, x1+bananas) and the X-shape (fish/pretzel and brezels). Recent analysis of x1+banana orbits by Portail et al. (2015b) and Qin (2016) shows that although this family is frequently invoked as causing the X-shape, these orbits do not appear except towards the ends of the bar and hence are probably not a significant contributor to the X-shape in the inner half of the bar. Furthermore, Qin (2016), who analysed the MW bar model presented by Shen et al. (2010), and classified orbits using a method based on orbital angular-momentum finds results completely consistent with those presented here. He compared the density images of the stacked orbital families to argue that

'x1-like' orbits (non-resonant but closer to the x1 resonant family) and 'boxy orbits' (box orbits showing larger deviations from x1 resonant family) contribute to different parts of peanut/X-shape.

In unsharp masked images, however, only fish/pretzels show a distinct, thin X-shape, while brezels show a more fuzzy X-shape. Although the unsharp masked images suggest that fish/pretzel orbits and brezel orbits contribute significantly, both families also contribute a significant fraction of their total mass outside the X-shape.

The non-resonant box orbits (which constitute 63 per cent of the mass of the bar), x1+banana orbits (3 per cent), fish-pretzels (6 per cent) and brezels (1.5 per cent) all show a distinct BP/X shape in projected surface density images, while only fish-pretzels and brezels (7.5 per cent in total) show the X-shape in unsharp masked images. This suggests that unsharp masking may underestimate the mass associated with the X-shape and that in fact the majority of bar orbits contribute to the BP/X shape.

In the next section, we see further evidence that the majority of orbits (especially the non-resonant box family) contribute to stellar number counts that provide evidence for a 3D BP/X-shaped bulge in the MW.

3.2 3D 'excess-mass' distribution

Using the method described in Section 2, we also computed the excess mass outside ellipsoids for each co-added orbit family in a manner similar to that carried out for the full model. Fig. 8 shows the excess mass outside ellipsoids for each co-added orbit family.

Table 1. Fraction of mass outside ellipsoids/orbits
contributing to X-shape.

Orbit	Fraction of mass outside ellipsoids
Model A	0.23
Model C	0.19
Boxes	0.25
X-tubes	0.10
x1+banana	0.33
3:−2:0	0.09
Brezel	0.28

When these maps are compared with Fig. 4 for the full simulations, it is clear that except for the *x*-tubes (top row middle panel) that shows only a hint of a BP/X-shape, all other orbit families show a clear BP/X shape suggesting that they all contribute to the 3D excess mass outside ellipsoids. The excess mass for each co-added orbit family is given in the second column of Table 1 and shows that all families in bar Model A contribute some fraction of their total mass to the BP/X-shaped region. Furthermore, Fig. 8 shows that each family contributes to the BP/X shape over a specific radial range: the resonant brezel and fish/pretzel orbits contribute closest to the centre of the bar within $|x| < 1.5$ kpc, the boxes contribute most significantly at intermediate radii, while the x1+banana orbits contribute primarily at the ends of the bar. In other words, the BP/X shape *is the bar* and the vast majority of orbits contribute to it.

3.3 Bimodal distribution in heliocentric distances

As discussed in the introduction, one of the first signatures of the 3D nature of the BP/X shape in the MW bulge was the detection of a bifurcation in RC star number counts as a function of magnitude (McWilliam & Zoccali 2010; Nataf et al. 2010) for $|b| \gtrsim 5°$. This bifurcation has been confirmed observationally by others (e.g. Saito et al. 2011) and is also found in simulations (e.g. Li & Shen 2012; Debattista et al. 2017).

We now examine the distributions of particles along various lines of sight for the full simulation and compare them with similar distributions for co-added orbits. To ensure that disc particles are excluded, we applied a cut that selects only particles that satisfy the constraint $(x/5)^2 + (y/1.5)^2 < 1$ (assuming that the semimajor axis length of the bar is 5 kpc and the semi-axis length in the disc plane is 1.5 kpc). No cut was applied perpendicular to the disc. All particles in a pencil beam with ± 0.25 kpc square cross-section were selected along four different lines of sight, at $l = 0°$ and $b = −4°, −5°, −6°, −7°$ (similar plots were obtained for $b = +4°, +5°, +6°, +7°$ but are not shown). The heliocentric distance distribution of particles in the HCR frame was fitted using a Gaussian Mixture Modelling (GMM) code (we use the PYTHON code sklearn.mixture.GMM available at http://scikit-learn.org that fits at most two Gaussian distributions to the distances of star particles along each line of sight. The code uses maximum-likelihood to estimate the parameters of the Gaussians.

In Fig. 9, the grey histograms show the number of star particles as a function of heliocentric distance along various lines of sight. The two solid curves show the Gaussians obtained from fitting the distribution of particles with the GMM code. The dashed curve shows the sum of the two Gaussians. The top row shows the distributions along four lines of sight for the full simulation: the locations of the means of the GMM Gaussians are marked with vertical lines, which are reproduced for reference at the same locations in the plots for co-added orbits in the next five rows. For the full simulation, the

histogram at $l = 0°, b = −4°$ is skewed with a single peak, similar to that observed in the MW. The GMM code fits the skewed distribution with two Gaussians with means separated by only 0.5 kpc but with very different standard deviations. For $b \leq −5°$, the bimodality is clearly visible in the histograms. Table 2 gives the separations between the means of the two Gaussians (from the GMM code) in kpc for the full simulation (top row) and each of the five co-added orbit families.

In the full simulation (top row of Fig. 9 and Table 2), we see that the separation of the peaks increases with increasing $|b|$ in a manner similar to that observed in the MW. This increase in the separation of the peaks in the number counts is regarded as evidence that our line of sight through the bar/bulge is passing through 'two opposing arms' of the X-shape that get farther apart as $|b|$ increases.

The *x*-tubes in the third row of Fig. 9 show no bimodality at any value of b, clearly indicating that they do not contribute to the 3D BP/X-shape (although they are probably contributed to the single peak at $b = −4$). Recall that *x*-tubes showed a clear peanut shape in projected distribution in Fig. 7.

Table 2 shows that only the box orbit family shows an increasing separation of peaks with increasing $|b|$ that closely matches the increasing separation of peaks seen in the full simulation. Furthermore, we see in Fig. 9 that only the peaks of the Gaussians for box orbits (second row) match the locations of the vertical lines (corresponding to the means of the Gaussians in the full simulation). In contrast, the resonant orbit families: 2:−2:1 x1+banana orbits (fourth row of Fig. 9), 3:−2:0 fish/pretzel (fifth row) and 3:0:−5 brezels (sixth row) show nearly constant separation in the peaks at all b values. In the case of the x1+banana and brezels, this is probably due to the shell-like structures seen in unsharp masked images for these two families shown in Fig. 7. For the 3:−2:0 fish/pretzel orbits (which show a slight increase in separation), it is probably due to the high degree of concavity of the arms of the X-shape. We also see from Table 2 that the separation of the peaks in the case of the x1+bananas is much larger at all b values than that observed in the full simulation, ruling out the possibility that this family is the dominant contributor to the bifurcation in stellar number counts. None the less, the x1+banana orbits definitely contribute to the tails of the distribution in the full simulation since the distributions in the other orbit families fall off more rapidly at small and large heliocentric distance than they do in the full simulation.

The conclusion that can be drawn from the analysis of the bimodal distribution of stars along various lines of sight is that stars on non-resonant box orbits, which are the dominant population in the bar, adequately account for both the bimodal distribution in RC stars and their increasing separation with increasing $|b|$. Since the resonant boxlet families show a bimodal distribution in heliocentric distance that is nearly independent of $|b|$, none of these families individually can explain the observations, although they contribute to the bimodality. In fact, it appears that the combination of non-resonant and resonant orbit families collectively produces the observed bimodal distribution in RC stars.

3.4 Line-of-sight kinematics of orbits

As mentioned previously, Vásquez et al. (2013) showed, using line-of-sight velocities for RC stars in the MW bulge, that stars on the near-side of the GC have more negative mean velocities than stars on the far side, a feature that is reproduced by Model A (Fig. 5). We now compare these results with co-added orbits from the five different families that were examined in previous sections.
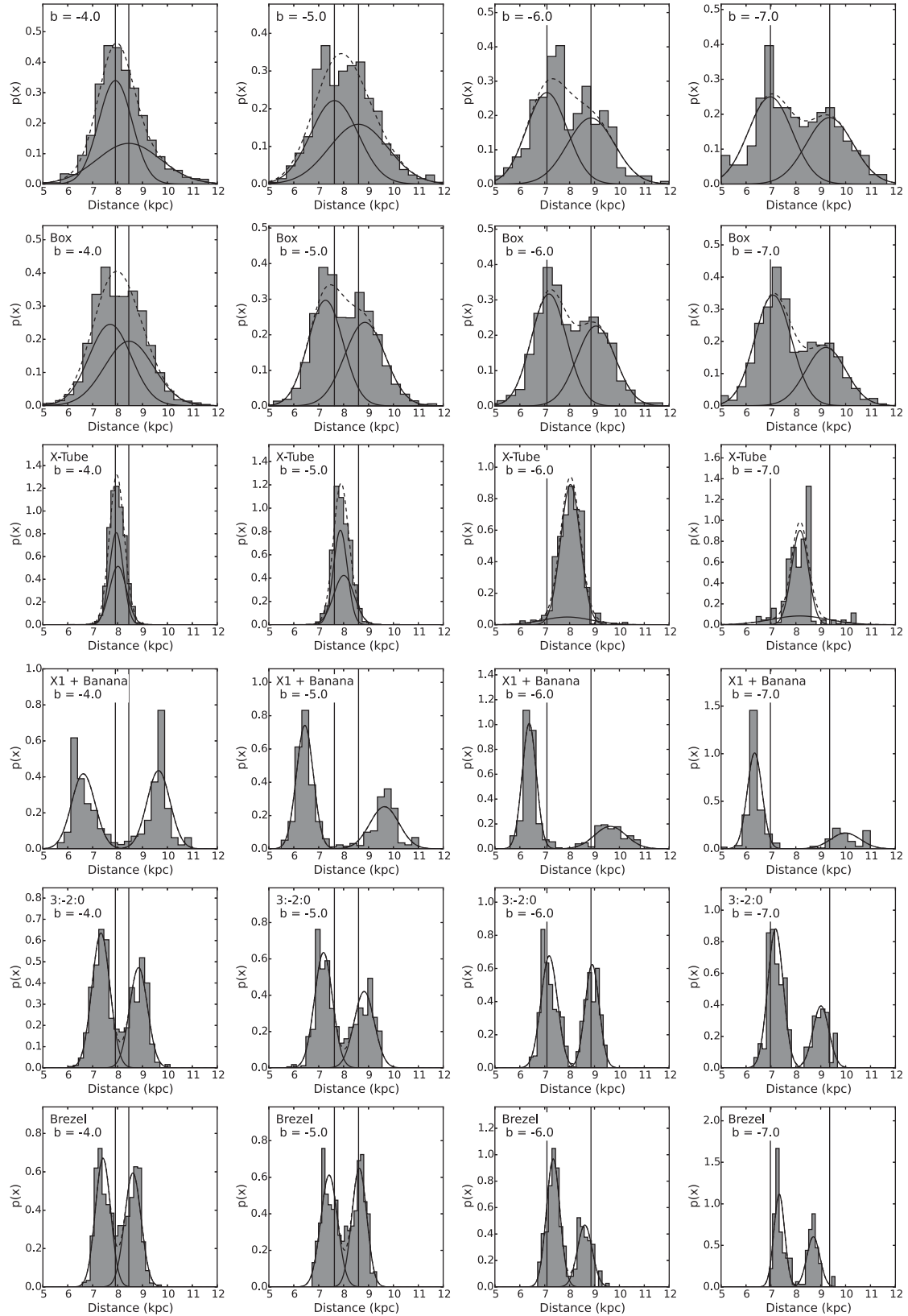
Figure 9. Normalized histograms showing number of stars along the line of sight as a function of heliocentric distance at $l = 0°$ and four different b values as indicated in the legends for the full simulation of Model A (top row) and five different orbit families also from Model A co-added (subsequent rows). Solid curves show the two Gaussians (see the text for details) that best fit the distribution and dashed curve shows the sum of the Gaussians. Vertical lines in the top row mark the locations of the means of the two Gaussians and these lines are reproduced in panels below. Only the peaks of the Gaussians for box orbits (second row) come close to matching the locations of the vertical lines.
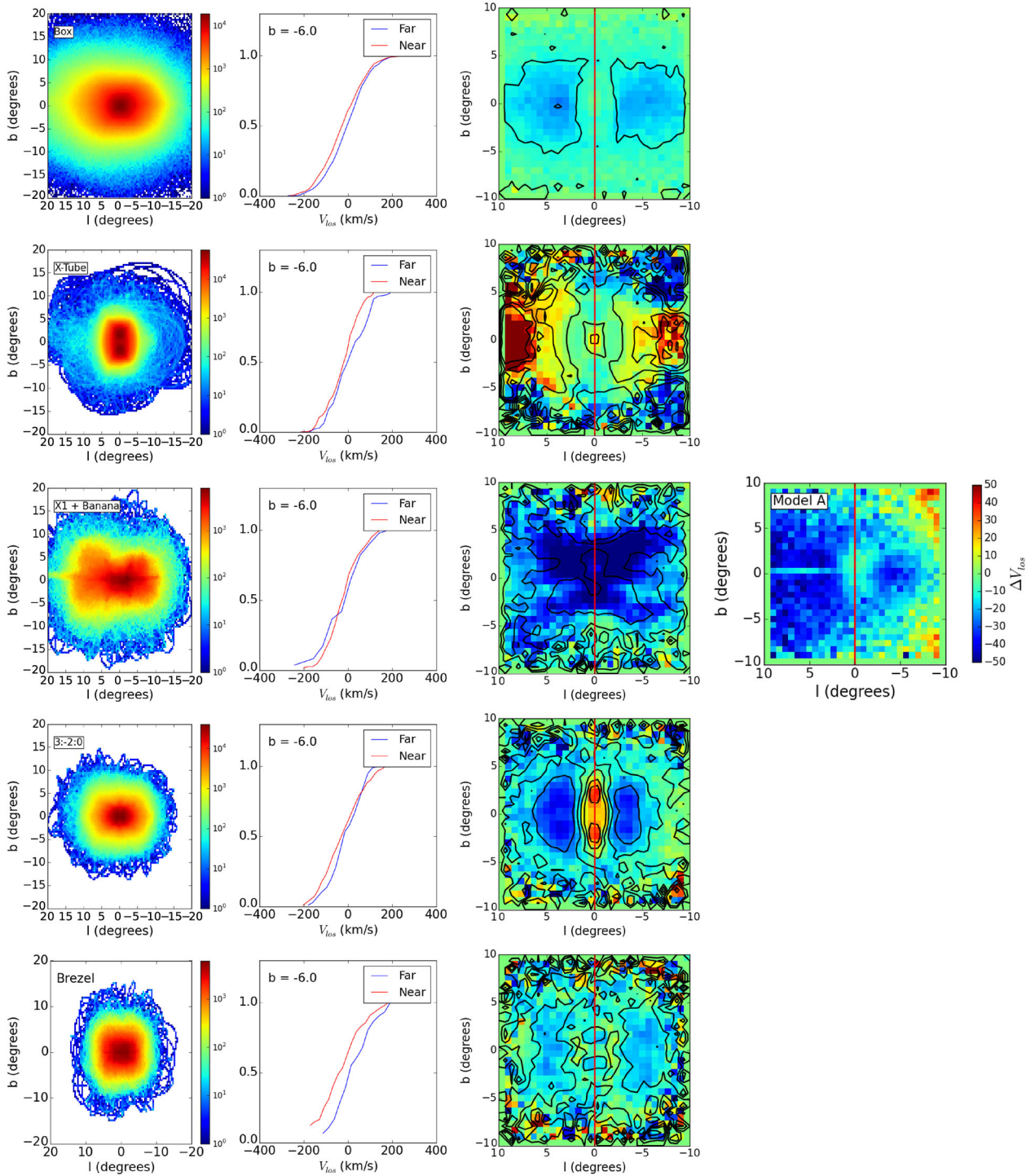
Figure 10. Left three columns: orbit projections as a function of l, b for co-added orbits belonging to five families in Model A. From top to bottom: boxes, x-tubes, x1+banana orbits, 3:−2:0 (fish/pretzels) and 3:0:−5 (brezels). The first column contains the projected density of the orbits viewed in the HCR frame. The second column shows the CDF of $V_{\rm los}$ for near (red) and far (blue) stars at $b = -6°$. The third column shows maps of the difference in the mean values of $V_{\rm los}$ for all l, b values in the bar region. Lastly, the image in the fourth column is the same as found in Fig. 5 in the fourth column.

Each row of Fig. 10 shows one co-added orbit family in the HCR frame. The first three columns show (from left to right) the projected density of stars, the CDFs of $V_{\rm los}$ for stars on the 'Near' (red) and 'Far' (blue) sides at $l = 0°$, $b = -6°$, and 2D maps showing $\Delta V_{\rm los}$ over the same range of l and b as in Fig. 5. (The 2D kinematic map for Model A is included in the third row, fourth

column to facilitate comparison with individual orbit families.) The first column of this figure shows that all the orbit families show some degree of asymmetry due to the projection effects arising from the orientation of the bar to our line of sight to the GC, but the x1+banana orbits show the greatest asymmetry (because they extend furthest out along the major axis).

The CDFs for individual orbits at $l = 0°$, $b = -6°$ (second column of Fig. 10) show only a small difference between the 'Near' and 'Far' side V_{los} providing little ability to discriminate between the different orbit families. Most orbit families qualitatively resemble the CDFs of Model A shown in Fig. 5, with the 'Near' (red) curve always leading the 'Far' (blue). The only exception is the x1+banana orbits where the blue curve leads at negative velocities, crossing over the red curve at $V_{los} \sim 0$. However, the velocity difference between 'Near' and 'Far' for all orbit families is smaller than it is for the full models and in the MW. It is not necessarily surprising that no individual orbit family shows the velocity difference observed in the MW or the full simulations, since the bars in these systems do not compris single orbit families, but the similarity between the CDFs for different families makes this a poor diagnostic. Fortunately, column 3 of Fig. 10 shows that there is much greater contrast between individual orbit families in 2D maps of ΔV_{los} than there is at a specific position (e.g. $l = 0°$, $b = -6°$ in column 2).

In fact, G14 and Qin et al. (2015) showed that 2D maps of ΔV_{los} for simulated bars with a strong BP/X-shape show an asymmetric ring-like structure with negative values of ΔV_{los} surrounding a central region with slightly positive or zero values at $l = 0°$, $b = 0°$. In contrast, bar simulations without an X-shape show vertical contours of ΔV_{los}.

A comparison with the ΔV_{los} map for Model A (fourth column, third row in Fig. 10) shows that no single orbit family fully accounts for the ring-like structure in the 2D map for Model A. Boxes (top row), $3:-2:0$ fish/pretzels (fourth row) and $3:0:-5$ brezels (fifth row) show similar structures to the full model. The x-tube orbits show a velocity signature that has the opposite sign of velocity relative to other orbit families and relative to Model A. The x1+banana orbits (fourth row) show a completely different 2D kinematic map with much more strongly negative velocities in a butterfly shape. However, only this last family produces the highly negative velocities at $5° < l < 10°$ and all b values. As mentioned previously, this family is found predominantly in the outer half of the bar and at this range of l values, the near-end of the bar is quite close to Sun, making this family very prominent in this part of the map.

Once again we find, from a comparison of 2D maps of ΔV_{los} of individual orbit families with the full simulation of Model A, that no single orbit family completely accounts for the BP/X-shape. The boxes and $3:-2:0$ and $3:0:-5$ resonant boxlets have similar overall shape in the 2D kinematic maps and account for most of the structure seen in the simulation. While the x1+banana family has a distribution on this map that is completely different from that of the full model and the other orbits, only this family produces the high negative ΔV_{los} values seen in the 2D map at large l. Thus, the 2D maps of the kinematics provide additional confirmation that all the non-resonant box and resonant boxlet families together contribute to the BP/X shape seen in the MW bulge.

4 SUMMARY AND CONCLUSIONS

In a previous paper (V16), we developed a new automated orbit classification algorithm to classify orbits in *N*-body bars using their fundamental orbital frequencies. In this work, we have used our previously published orbit classification for an *N*-body bar (scaled to fit BRAVA kinematics of the MW bulge) to determine which orbit family or families are primarily responsible for the BP and X-shape seen in the MW bulge. Although the bar model we present in this paper was not tailored to fit observations in the MW, it shows numerous similarities both in kinematics and in spatial distribution of stars contributing to the X-shape, enabling us to draw inferences

Table 2. Separation of peaks in heliocentric distances of star particles along four lines of sight.

	$b = -4°$ (kpc)	$b = -5°$ (kpc)	$b = -6°$ (kpc)	$b = -7°$ (kpc)
Model A (full)	0.5	1.0	1.8	2.4
Boxes (63 per cent)	0.8	1.6	1.9	2.1
X-tube (8.5 per cent)	0.1	0.1	0.1	0
x1+banana (3 per cent)	3.	3.2	3.3	3.7
$3:-2:0$ (5.9 per cent)	1.5	1.6	1.7	1.8
Brezel (1.4 per cent)	1.2	1.2	1.3	1.4

about the nature of the orbits that might constitute the MW bar. The results presented here should be followed up in the future by a similar analysis of a self-consistent model that is specifically tailored to fit the MW bar. We assess the importance of various orbit families to the structure of the X-shape by examining four different diagnostics for the full simulation and the co-added orbit families: (1) the projected density distributions and unsharp masked images, (2) projected 3D distribution of the 'excess-mass' outside ellipsoids, (3) the radial distribution of stars along several lines of sight and (4) 2D maps showing ΔV_{los}, the difference in line-of-sight velocity between stars on the 'Near' and 'Far' sides of the GC. We summarize our main findings below.

(i) Our examination of co-added orbit families using edge-on projected density distributions and unsharp masked images (Fig. 7) shows that the main contributors to the BP shape in projected density maps for our *N*-body model are non-resonant box orbits (which constitute ~60 per cent of bar orbits), long-axis (x) tubes (8.5 per cent of bar orbits) and resonant boxlet families: $3:-2:0$ 'fish/pretzel' resonance (6 per cent of bar orbits), $3:0:-5$ 'brezel' orbits (1.5 per cent) and $2:-2:1$ x1+banana orbits (3 per cent).

(ii) In contrast, a clear X-shape in unsharp masked images is produced only by the resonant boxlet families associated with the $3:-2:0$ resonance and the $3:0:-5$ resonance. While the resonant x1+banana orbits show a clear BP/X-shape in projection, they show a double shell-like structures at ± 2 kpc in unsharp masked images but no X-shape.

(iii) In a manner similar to that employed by Portail et al. (2015a), the fraction of mass associated with the X-shape is determined by computing several isodensity surfaces and subtracting the mass of an ellipsoid that lies entirely within each surface. This method yields a mass fraction associated with the BP/X-shape of 23 per cent in Model A and 19 per cent in Model C comparable to that found by Portail et al. (2015a, 24^{+5}_{-4} per cent). Fig. 4 shows that both models show a clear BP/X shape when the excess mass is projected on to the x–z plane. A similar analysis carried out for co-added orbits in Model A finds excess masses ranging from 10 per cent for x-tubes to 25 per cent for non-resonant boxes and 33 per cent for x1+banana orbits, confirming that all the orbit families considered contribute to the 3D BP/X-shape. Fig. 8 shows that box orbits, x1+banana orbits, fish/pretzel orbits and brezels all show X-shapes in their 3D excess-mass distributions, with each orbit family contributing to the X-shape over a different radial range.

(iv) The bifurcation in the distributions in RC star number counts as a function of observational magnitude (McWilliam & Zoccali 2010; Nataf et al. 2010) for $|b| \gtrsim 5°$ is a prominent signature of the 3D structure of the MW's X-shaped bulge. In the MW bulge and the full simulation (top row of Fig. 9 and Table 2), the increasing separation of the peaks of the number count distribution with increasing $|b|$ is evidence that our line of sight through the MW bulge is

passing through two opposing arms of the X-shape that get farther apart as $|b|$ increases. A comparison with co-added orbit families shows that only the box orbit family shows such an increasing separation of peaks with increasing $|b|$ (Fig. 9 and Table 2), while the resonant orbit families (3:−2:0 fish/pretzel, 3:0:−5 brezels and 2:−2:1 x1+banana orbits) show nearly constant separation in the peaks at the four b values examined. Furthermore, x1+banana orbits show a much greater separation of peaks (∼3 kpc) at all b values than observed in the full simulation.

(v) The difference between the line-of-sight velocities of stars on the 'Near' and 'Far' sides of the GC in the MW at $l = 0°$, $b = −6°$ is observed to be about $50\,\mathrm{km\,s^{-1}}$. We see a similar velocity signature but with a smaller velocity difference of ∼$24\,\mathrm{km\,s^{-1}}$ in the full simulations. Most of the co-added orbit families show a small velocity difference at this specific l, b value (Fig. 10 middle column), providing no discriminatory potential.

(vi) In 2D kinematic maps (Fig. 10 right-hand column), the velocity difference between 'Near' and 'Far' side stars for N-body simulations with X-shapes shows a distinctive asymmetric ring-shaped region of negative ΔV_{los} surrounding a region with slightly positive or zero values at $l = 0°$, $b = 0°$ (G14). The 2D kinematic maps for the co-added orbits for box and boxlet families show overall similarity to the structure seen in the full simulation except at $5° < l < 10°$ (the near-end of the bar) where only x1+banana orbits produce sufficiently negative ΔV_{los}.

In summary, our use of four different diagnostics to compare co-added orbit families with the full simulations shows that the BP/X shape in our N-body model is produced largely by the box orbit family that constitutes the majority of orbits in the bar. Although resonant families such as the 2:−2:−1 x1v1 (banana), 3:−2:0 fish/pretzels and 3:0:−5 brezels contribute to the BP and X-shapes in projected density maps, none of these families is individually able to account for the increasing separation with increasing $|b|$ of the radial stellar number counts and the asymmetric ring structure of the 2D kinematic maps. These results suggest that the non-resonant box orbits, in conjunction with the resonant boxlets, are *collectively* responsible for all the observed features of the BP/X-shape seen in the MW bulge.

It is not entirely surprising that the box orbits and resonant boxlets constitute the major families making up the BP shape and the X-shapes seen in our bar simulation. Non-resonant box orbits comprise of three independent fundamental orbital frequencies. Valluri et al. (2010) studied a triaxial potential primarily comprising box orbits as it was deformed by the addition of baryons to a more spherical/oblate potential. They found that despite the dramatic increase in oblateness at small radii, the overall orbit populations in this region did not change very significantly, but rather the box orbits at small radii adiabatically deformed to become much rounder. In other words, since box orbits have three independent orbital fundamental frequencies, each frequency can be changed independently of the others, allowing these orbits to easily change shape as the underlying potential is modified.

It is as yet uncertain whether the BP/X shape seen in edge-on bars arises from the rapid buckling instability of the bar or whether it arises from more the adiabatically varying potential change associated with resonant trapping. Regardless of the process by which these structures form, since non-resonant box orbits are the backbones of bars (V16), they readily adapt to potential change in a manner similar to Lissajous figures.

Recent analysis of the kinematics of ∼2000 giant stars in the direction of the Galactic bulge, obtained by the *Gaia*-ESO survey,

shows differences in the line-of-sight velocity dispersions of metal-poor and metal-rich stars, which these authors argue point to the metal-rich stars being on banana orbits (Williams et al. 2016). Our comprehensive analysis of orbits in an N-body bar shows that the banana orbit family is not capable of reproducing all spatial and kinematic characteristics associated with the X-shape. Future analysis of the orbits of stars in hydrodynamical simulations of bars could lead to additional insights into correlations between metallicity, kinematics and orbit type, perhaps enabling us to distinguish between the two main formation mechanisms, bar buckling and resonant orbit trapping.

REFERENCES

Araki S., 1985, PhD thesis, MIT
Athanassoula E., 2002, ApJ, 569, L83
Athanassoula E., 2005, MNRAS, 358, 1477
Athanassoula E., Bienayme O., Martinet L., Pfenniger D., 1983, A&A, 127, 349
Binney J., Tremaine S., 2008, Galactic Dynamics: Second Edition. Princeton Univ. Press, Princeton, NJ
Blitz L., Spergel D. N., 1991, ApJ, 379, 631
Brown J. S., Valluri M., Shen J., Debattista V. P., 2013, ApJ, 778, 151
Burbidge E. M., Burbidge G. R., 1959, ApJ, 130, 20
Bureau M., Athanassoula E., 2005, ApJ, 626, 159
Bureau M., Aronica G., Athanassoula E., Dettmar R.-J., Bosma A., Freeman K. C., 2006, MNRAS, 370, 753
Ciambur B. C., Graham A. W., 2016, MNRAS, 459, 1276
Combes F., Sanders R. H., 1981, A&A, 96, 164
Combes F., Debbasch F., Friedli D., Pfenniger D., 1990, A&A, 233, 82
Contopoulos G., Papayannopoulos T., 1980, A&A, 92, 33
de Zeeuw T., 1985, MNRAS, 216, 273
Debattista V. P., Carollo C. M., Mayer L., Moore B., 2005, ApJ, 628, 678
Debattista V. P., Mayer L., Carollo C. M., Moore B., Wadsley J., Quinn T., 2006, ApJ, 645, 209
Debattista V. P., Ness M., Gonzalez O. A., Freeman K., Zoccali M., Minniti D., 2017, MNRAS, 469, 1587
Dehnen W., 1993, MNRAS, 265, 250
Eisenhauer F., Schödel R., Genzel R., Ott T., Tecza M., Abuter R., Eckart A., Alexander T., 2003, ApJ, 597, L121
Freudenreich H. T., 1998, ApJ, 492, 495
Gajda G., Łokas E. L., Athanassoula E., 2016, ApJ, 830, 108
Gardner E., Debattista V. P., Robin A. C., Vásquez S., Zoccali M., 2014, MNRAS, 438, 3275

Kunder A. et al., 2012, AJ, 143, 57

Laurikainen E., Salo H., Buta R., Knapen J. H., 2011, MNRAS, 418, 1452

Li Z.-Y., Shen J., 2012, ApJ, 757, L7

Li Z.-Y., Shen J., 2015, ApJ, 815, L20

Lütticke R., Dettmar R.-J., Pohlen M., 2000, A&AS, 145, 405

McWilliam A., Zoccali M., 2010, ApJ, 724, 1491

Martinez-Valpuesta I., Shlosman I., 2004, ApJ, 613, L29

Martinez-Valpuesta I., Shlosman I., Heller C., 2006, ApJ, 637, 214

Nataf D. M., Udalski A., Gould A., Fouqué P., Stanek K. Z., 2010, ApJ, 721, L28

Nataf D. M. et al., 2015, MNRAS, 447, 1535

Ness M., Lang D., 2016, AJ, 152, 14

Ness M. et al., 2012, ApJ, 756, 22

O'Neill J. K., Dubinski J., 2003, MNRAS, 346, 251

Patsis P. A., Katsanikas M., 2014a, MNRAS, 445, 3525

Patsis P. A., Katsanikas M., 2014b, MNRAS, 445, 3546

Patsis P. A., Xilouris E. M., 2006, MNRAS, 366, 1121

Patsis P. A., Athanassoula E., Grosbøl P., Skokos C., 2002a, MNRAS, 335, 1049

Patsis P. A., Skokos C., Athanassoula E., 2002b, MNRAS, 337, 578

Pfenniger D., Friedli D., 1991, A&A, 252, 75

Portail M., Wegg C., Gerhard O., Martinez-Valpuesta I., 2015a, MNRAS, 448, 713

Portail M., Wegg C., Gerhard O., 2015b, MNRAS, 450, L66

Portail M., Gerhard O., Wegg C., Ness M., 2017, MNRAS, 465, 1621

Qin Y., 2016, MS thesis, Shanghai Astronomical Observatory, Chinese Academy of Sciences

Qin Y., Shen J., Li Z.-Y., Mao S., Smith M. C., Rich R. M., Kunder A., Liu C., 2015, ApJ, 808, 75

Quillen A. C., 2002, AJ, 124, 722

Quillen A. C., Minchev I., Sharma S., Qin Y.-J., Di Matteo P., 2014, MNRAS, 437, 1284

Raha N., Sellwood J. A., James R. A., Kahn F. D., 1991, Nature, 352, 411

Rich R. M., Reitzel D. B., Howard C. D., Zhao H., 2007, ApJ, 658, L29

Rowley G., 1988, ApJ, 331, 124

Saito R. K., Zoccali M., McWilliam A., Minniti D., Gonzalez O. A., Hill V., 2011, AJ, 142, 76

Sellwood J. A., 2014, preprint (arXiv:1406.6606)

Sellwood J. A., Valluri M., 1997, MNRAS, 287, 124

Shaw M. A., 1987, MNRAS, 229, 691

Shen J., Sellwood J. A., 2004, ApJ, 604, 614

Shen J., Rich R. M., Kormendy J., Howard C. D., De Propris R., Kunder A., 2010, ApJ, 720, L72

Skokos C., Patsis P. A., Athanassoula E., 2002a, MNRAS, 333, 847

Skokos C., Patsis P. A., Athanassoula E., 2002b, MNRAS, 333, 861

Skrutskie M. F. et al., 2006, AJ, 131, 1163

Valluri M., Merritt D., 1998, ApJ, 506, 686

Valluri M., Debattista V. P., Quinn T., Moore B., 2010, MNRAS, 403, 525

Valluri M., Shen J., Abbott C. G., Debattista V. P., 2016, ApJ, 818, 141

Vásquez S. et al., 2013, A&A, 555, A91

Wegg C., Gerhard O., 2013, MNRAS, 435, 1874

Wegg C., Gerhard O., Portail M., 2015, MNRAS, 450, 4050

Williams A. A. et al., 2016, ApJ, 824, L29

This paper has been typeset from a TEX/LATEX file prepared by the author.